Engineering Structures 304 (2024) 117667

Contents lists available at ScienceDirect

Engineering Structures

journal homepage: www.elsevier.com/locate/engstruct

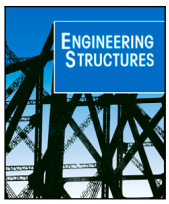

Effects of topographic irregularity on seismic site amplification considering input signal frequency: A case study

Zhe-Xing Chen [a], Guan Chen [a,b,*], Yong Liu [a]

[a] State Key Laboratory of Water Resources Engineering and Management, Wuhan University, Wuhan 430072, PR China
[b] Institute for Risk and Reliability, Leibniz Universität Hannover, Hannover 30167, Germany

ARTICLE INFO

Keywords:
Topographic irregularity
Seismic response
Ground motion
Frequency
Site amplification

ABSTRACT

The topographic amplification effect has significant impacts on structural safety since it causes inconsistencies in seismic response. Previous studies on topographical influence focus on a certain point and cross-sections, which is insufficient to comprehensively understand the topographic amplification effect. Besides, few studies analyze the relationship between seismic response and ground motion frequency. Hence, this study aims to investigate the effects of topographic irregularity of the whole site, and explore the relationship between seismic response characteristics and signal frequency. An analysis procedure for modeling and meshing an actual 3D site is proposed by combining SolidWorks, SketchUp and Abaqus. Finite element method (FEM) is applied to simulate the seismic response. Results show that the site amplification and de-amplification are associated with topographic features. Specifically, the seismic responses of ravine and ridge areas could differ by a factor of two. However, acceleration response in ravine areas shows unusual amplification under input signal frequencies over 4 Hz. Besides, the frequency of input ground motion certainly affects the seismic site amplification. Specifically, in this study, the seismic response peaks when the input frequency is in the range of 0.4–0.8 Hz, which corresponds to the resonance frequency of the numerical model. In terms of frequency, site amplification showed a correlation between actual recordings and artificial signal inputs, but lower intensities are observed when actual records are input. Therefore, the engineering risk will be underestimated when the topographic irregularity and frequency characteristic of input ground motion are inappropriately considered. The findings of this study provide a new approach to investigate the actual 3D site amplification effects and shed new insight on regional seismic risk analysis.

1. Introduction

The intensity of seismic ground motion is related to the terrain. Specifically, the topographic amplification effect leads to non-uniform ground responses, which result in the spatial variability of seismic records. For example, in the 2011 Tohoku earthquake, the acceleration time histories recorded at the Tatsumi and Hachieda stations, which are 800 meters apart, showed significant differences [1]. Non-uniform seismic responses caused by the topographic amplification effect could worsen earthquake consequences, such as geologic secondary disasters and building collapse. For example, more than 3400 landslides covering an area of 6.9 square kilometers were triggered by the 2016 Kumamoto earthquake in Japan [2]. In the 2009 L'Aquila earthquake, the city of L 'Aquila and several small villages along the Aterno Valley suffered heavy damage with 308 deaths, 1600 injured and 40,000 left homeless [3]. The Hokkaido Eastern Iburi earthquake of 2018 (M-JMA 6.7) led to strong ground motions and coseismic landslides, which resulted in the death of over 40 people, injuries exceeding 700, and partial or complete destruction of more than 2000 buildings [4]. Therefore, the effects of topographic irregularity on seismic site response play a crucial role in seismic hazard and risk analysis.

The seismic site response is a complex issue and affected by various factors, such as the depth of strata, bedrock properties, soil deposit thickness, average shear wave velocity to seismic bedrock, index properties of the strata, over-consolidation ratio and effective stress. Various work also has been done to explore this issue. For example, Rathje et al. [5] quantified the uncertainties of input motion and soil properties on seismic site response with different soil conditions. The influences of linearity and nonlinearity of the medium [6], dynamic parameters like damping [7], bedrock properties [8], the plasticity index of the soil [9,10] are also widely investigated. Furthermore, researchers have optimized classification schemes for a site's stratigraphic soil conditions [11–13]. This study focuses on the effects of topographic

* Corresponding author at: Institute for Risk and Reliability, Leibniz Universität Hannover, Hannover 30167, Germany.
E-mail addresses: chenzhx@whu.edu.cn (Z.-X. Chen), guan.chen@irz.uni-hannover.de (G. Chen), liuy203@whu.edu.cn (Y. Liu).

https://doi.org/10.1016/j.engstruct.2024.117667
Received 26 October 2023; Received in revised form 3 January 2024; Accepted 11 February 2024
Available online 17 February 2024

irregularity and input signal frequency. To date, some work on the input direction and the site characteristics have been investigated [14–16]. The effects of frequency on seismic response amplification are also discussed. For example, Paolucci [17] emphasized the great influence of resonance on earthquake investigation. However, seismic site response considering input ground motion frequencies and topography remains largely unexplored. The objective of this study is to explore the effects of tomographic irregularity on seismic site amplification subjected to artificial and recorded excitation with various frequencies, where an actual 3D site is adopted as an example.

Various methods in seismic site response analysis are developed, such as centrifuge shaking table testing, 1 g shaking table testing, and numerical simulation method. These methods have reached a certain level of maturity in site analysis nowadays. However, they still inevitably have certain limitations and operational difficulties [18]. For example, experiments has advantages in providing realistic representations, validating models, and enabling direct measurements, while disadvantages encompass limitations in scale, cost, and the challenge of replicating all relevant factors found in natural settings. By contrast, over the past several decades, with the continuous improvement of computational capabilities and advances in computational methods, numerical simulation has been extensively used in seismic analysis.

2D and 3D analysis strategies for examining seismic responses in real-world sites are widely used in previous work [19–23]. The limitations of conventional 1D [19] and 2D [20,21] approaches have been acknowledged, emphasizing the significance of employing 3D models to explore the impacts of terrain irregularities [22,23]. Accurate seismic response reproductions now consider factors such as stratigraphic anisotropy and plasticity, as highlighted in recent studies on diverse locations, including Turkey [24], borehole sites [25], hilly regions [26], and Kathmandu [27]. Recognizing the subjectivity and restrictions inherent in traditional methods relying on observation points or confined to 2D cross-sections, there is a recognized need for improvement. While focusing on specific points and sections can enhance efficiency, it may overlook certain phenomena in actual sites. For instance, Muñoz and Sáez [19] advocate for the superior accuracy and reliability of 3D analysis strategies compared to 1D approaches. Similarly, Pasqua [20] notes that earthquake analyses based on 2D cross-sections may underestimate the amplification effect of shaking, particularly in 3D terrain with mountain peak branches.

A limited number of studies have undertaken seismic response analyses considering the entire study site, with even fewer addressing topographic effects. Connecting seismic responses to actual topography becomes crucial for complex terrain site engineering. Studies covering adjacent valleys [28], regular basins [29], V-shaped valleys [15,30], ridges, slopes [31], and large-scale topographic features have been explored [32]. Chen et al. [32] investigated the statistical relationship between the topographic amplification effect and ground concave–convex features at large scales. Additionally, understanding patterns associated with smaller-scale topographic features is considered essential for aiding engineering construction and explaining specific engineering phenomena [32–36].

The modeling and meshing of a 3D numerical site is the key to simulating seismic site response. Terrain modeling consists of two parts: site model building and model meshing. In the site model building stage terrain generation is difficult if the method is complex. However, efficient methods can negatively affect the efficiency of subsequent meshing and computation. The Point cloud topography generation, as the critical step of modeling, includes various methods, such as marching cube [37], grid [38], and triangular irregular network (TIN) [39]. Notably, the marching cube offers detailed modeling, albeit at a high computational cost. However, open-source DEM data do not support detailed modeling. In response to the limitation of data and according to the demand, TIN is used as a suitable method for terrain modeling due to its efficiency and reliability [39]. A process of terrain generation and elements division is summarized. Elements division is extremely critical for computational speed, and virtual topology is employed to make hexahedral meshes available to reduce computational time. The subsequent procedures and advantages of saving computing resources are elucidated in the following sections of this study. The proposed process makes the meshing of the site model formed by triangulation feasible and minimizes the computational requirements of the meshed results.

Tibetan Plateau, as one of the most active tectonics plate with tons of river valleys on earth [40], has complex geological conditions, which brings energy and source materials to geological disasters, such as earthquakes, landslides and land subsidence [41–44]. Hence, a typical area in Tibetan Plateau (see Fig. 1) is taken as an example in this study to investigate the effects of tomographic irregularity and signal frequency.

This study aims to uncover the relationship between terrain and the seismic response, summarize the pattern of seismic response intensity on the different topographical characteristics, and investigate the correlation between seismic response intensities and input signal frequencies by introducing input signal frequencies to irregular topographic seismic responses. A modeling process is assembled to analyze the seismic site amplification of an actual site. Additionally, the results of whole-site seismic responses and the response intensities under different input signal frequencies are investigated, which could contribute to estimate seismic responses of complex large-span engineering structures.

2. Methodology

2.1. Finite element analysis

Modeling seismic signal propagation in a finite domain has posed a longstanding dynamic challenge. The finite element method, while suitable for solving problems in a continuum, presents limitations when analyzing scenarios involving large deformations. However, as this study specifically focuses on surface response without delving into large deformations, the finite element method is used. The preprocessing and meshing of intricate models significantly impact the reliability of finite element method results, prompting us to propose a streamlined procedure for modeling and meshing simplification. Additionally, challenges arise in establishing reflection-free boundaries within the finite domain and accurately inputting seismic signals in simulating seismic site response using the finite element method. To address these challenges, this study introduces viscoelastic boundaries and equivalent nodal forces.

2.1.1. Viscoelastic artificial boundary

The boundary of a study needs to be suitably chosen since the research area of a study is certain, but the seismic signals propagate in semi-infinite space. Imposing an artificial boundary on the study area can simulate the propagation characteristics of the pulse in semi-infinite space at the boundary without reflecting at the truncated boundary of the study area. The viscoelastic artificial boundary is set on this 3D terrain model to simulate the seismic wave propagation [29,45].

Deeks and Randolph [45] proposed the viscoelastic boundary, then Liu et al. [46]improved it. The viscoelastic artificial boundary consists of a continuous distributed spring damping system on the artificial truncation boundary. The engineering characteristics at boundary nodes are shown in Fig. 2. The mechanical parameters of springs and dampers are determined by the surrounding rock materials, given as Eq. (1):

$$\begin{cases} K_{\mathrm{BT}} = \alpha_{\mathrm{T}} \dfrac{G}{R}, C_{\mathrm{BT}} = \rho C_{\mathrm{S}} \\ K_{\mathrm{BN}} = \alpha_{\mathrm{N}} \dfrac{G}{R}, C_{\mathrm{BN}} = \rho C_{\mathrm{P}} \end{cases} \tag{1}$$

where K_{BN} and C_{BN} are the radial spring constant and damping constant, respectively; K_{BT} and C_{BT} are the tangential spring constant and damping constant, respectively; G and ρ are the soil shear modulus

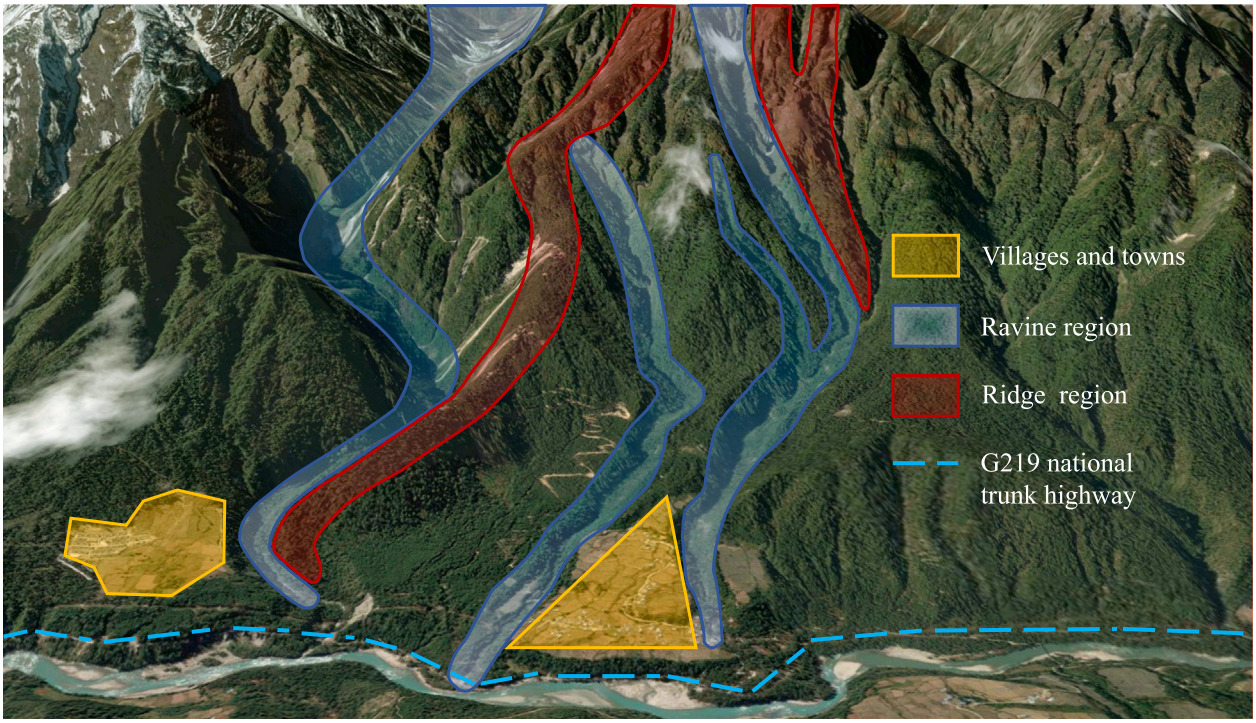

Fig. 1. Typical ravines and ridges on mountain sidewalls in research area.

and mass density at boundary nodes that require springs and dampers, respectively; α_T, α_N are the correction coefficients of the viscoelastic boundary, and in the two-dimensional case, the values of α_T and α_N refer to the study of Liu et al. [46]; $\alpha_T = 0.5$, $\alpha_N = 1$; R is the distance from the scattered wave source to the artificial boundary node. C_S and C_P are the shear wave velocity and longitudinal wave velocity of the medium, respectively.

The nodal information of the truncated boundary for relatively complex terrain is extracted to calculate the required position information when applying the viscoelastic boundary. Then, by applying a fully fixed constraint with unit pressure to the truncated boundary, the support reaction force of the fixed support at each node is calculated, and the value of this reaction force is the nodal control area. G, C_S and C_P mentioned in Eq. (1) are expressed as Eq. (2).

$$\begin{cases} G = \frac{E}{2(1+\nu)} \\ C_S = \sqrt{\frac{G}{\rho}} = \sqrt{\frac{E}{2\rho(1+\nu)}} \\ C_P = \sqrt{\frac{\lambda+2G}{\rho}} = \sqrt{\frac{E(1-\nu)}{\rho(1+\nu)(1-2\nu)}} \end{cases} \tag{2}$$

where E and ν are the elastic modulus and Poisson's ratio of the medium, and λ is the first lame constant. Wave velocity calculations are given here only for elastic materials, as they are used in this study.

2.1.2. Equivalent nodal load

Equivalent nodal load can ensure stress input continuity and high accuracy at the artificial boundary [47]. Therefore, the seismic waves input by the equivalent nodal load method are introduced into the model. For any node b of the boundary, the magnitude of the equivalent nodal load F_b is expressed as Eq. (3) [29]:

$$F_b = (K_b u_b^{ff} + C_b \dot{u}_b^{ff} + \sigma_b^{ff} n) A_b \tag{3}$$

where $K_b u_b^{ff}$ is to overcome the additional stress due to the displacement of the spring unit; $C_b \dot{u}_b^{ff}$ is to overcome the additional stress due to the velocity of the damper; $\sigma_b^{ff} n$ is the stress tensor due to the free field vibration at the boundary. $u_b^{ff} = [u\ v\ w]$ is the incident wave displacement vector; $\dot{u}_b^{ff} = [\dot{u}\ \dot{v}\ \dot{w}]$ is the incident wave velocity vector; A_b is the boundary node control region; n is the normal cosine vector outside the boundary; K_b, C_b are the spring stiffness and damping coefficients on the viscoelastic boundary, respectively. In the two-dimensional case, the displacement vector of the incident wave at the boundary node is $u_b^{ff} = [u\ v]$, and the velocity vector of the incident wave is $\dot{u}_b^{ff} = [\dot{u}\ \dot{v}]$.

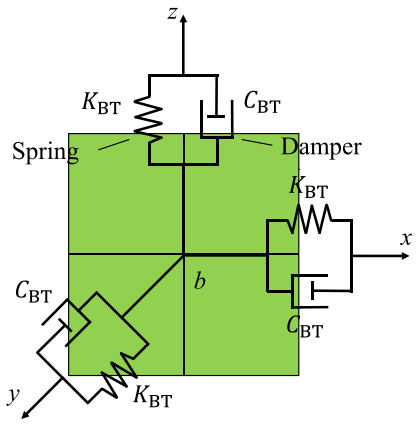

Fig. 2. Schematic of the artificial boundary engineering features at arbitrary boundary node b. K_{BN} and C_{BN} are the radial spring constant and damping constant, respectively; K_{BT} and C_{BT} are the tangential spring constant and damping constant, respectively.

The viscoelastic boundary and equivalent nodal loads can be automatically applied to the boundary nodes. The program flowchart is shown in Fig. 3.

2.1.3. Validation

As shown in Fig. 4(C), a symmetric V-shaped valley with depth d and half-width b is established for methods validation. The dimension parameters are illustrated in Fig. 4(A), where half-width b = 20 m, depth d = 20 m, local near-field dimensions x = 1200 m, y = 100 m (width is 1200 m, height is 100 m). Mean-valued elastic materials are used to model.

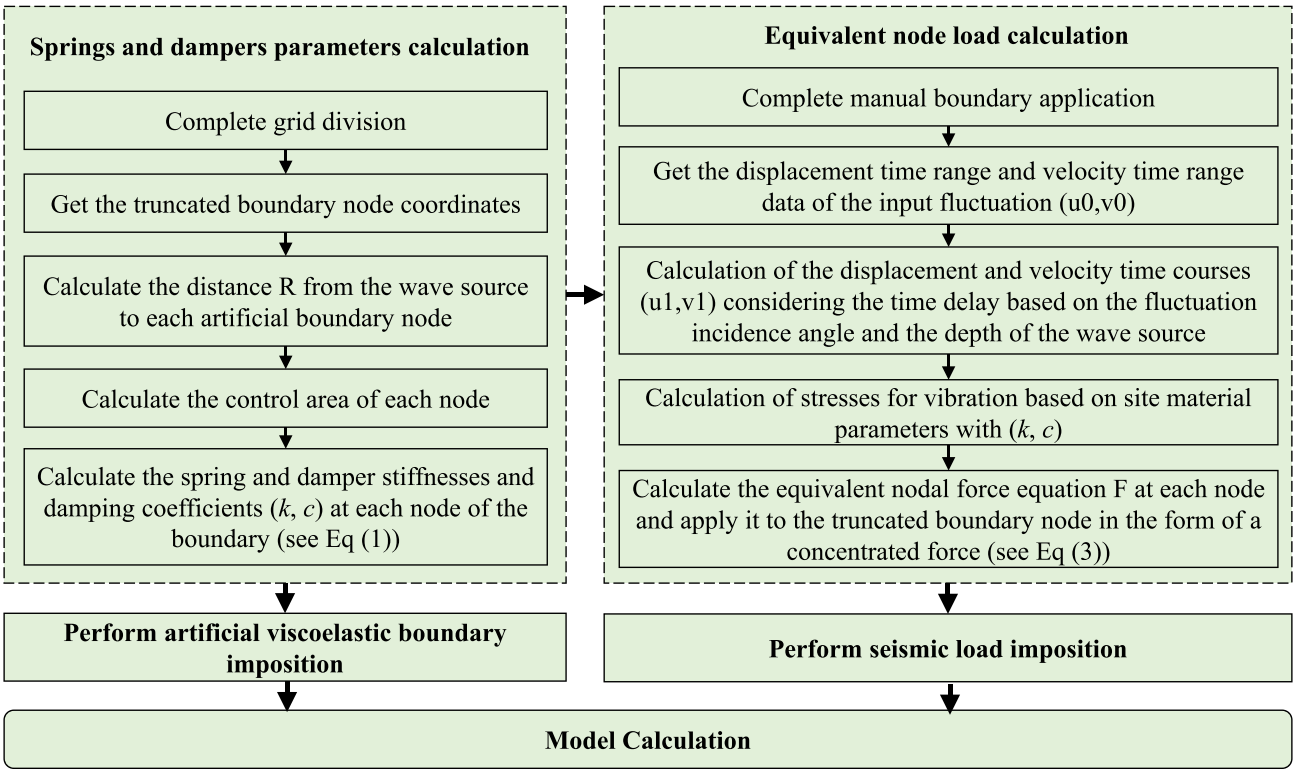

Fig. 3. Artificial boundary and seismic load imposition process.

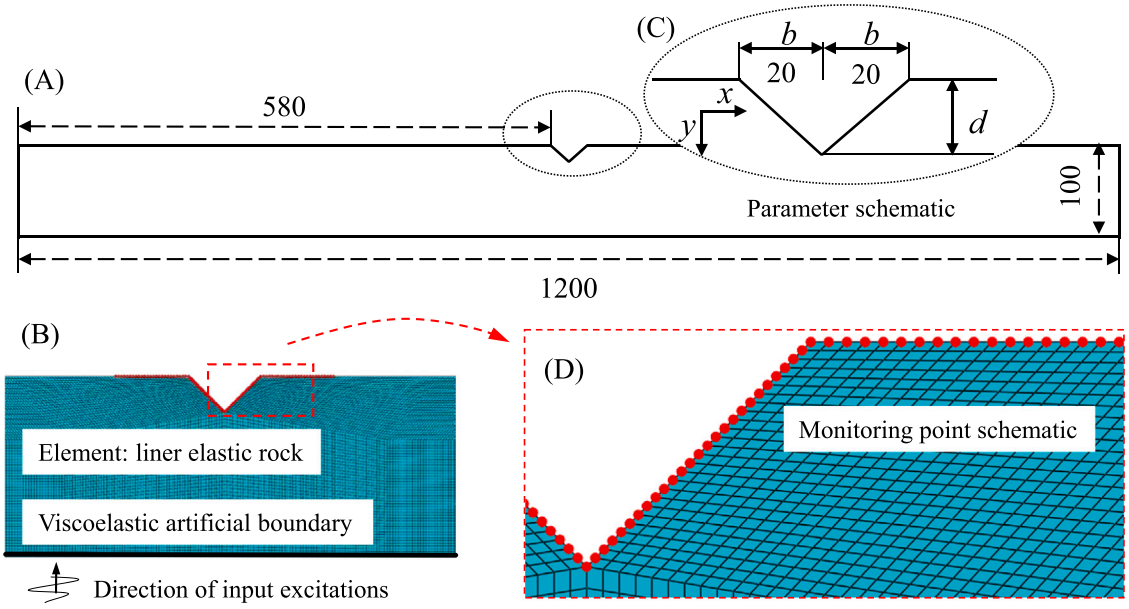

Fig. 4. 2D canyon site model used for model validation. (A) Overall model dimensions, (B) Near-field grid division, the artificial boundary and the earthquake input direction, (C) The model parameters, (D) Schematic diagram of the monitoring point locations.

For seismic waves to be accurately propagated, we refer to the work of Liu et al. [29] and the analysis from Kuhlemeyer and Lysmer [48]. The longest element size in the direction of seismic propagation should satisfy the requirements of Eq. (4).

$$h_{\max} = \frac{1}{10} \sim \frac{1}{8}\left(\frac{V_S}{f_{\max}}\right) \tag{4}$$

where $h_{\max}$ is the largest size for the grid, V_S is the shear wave velocity of soil, $f_{\max}$ is the maximum input signal frequency.

A linear elastic material is used, and the material parameters are shown in Table 1. The model is discretized using 52 920 elements, and the element division of the model is shown in Fig. 4(B). The element type used is four-node plane strain element with reduced integration (CPE4R), which is a suitable type for 2D plane strain problems without

Table 1
Material parameters of the simulated model.

Material property	Mass density	Poisson ratio	Young's modulus	Shear modulus	SH-wave velocity
Elasticity	2670 kg/m^3	0.25	1.66857×10^9 Pa	6.67428×10^8 Pa	500 m/s

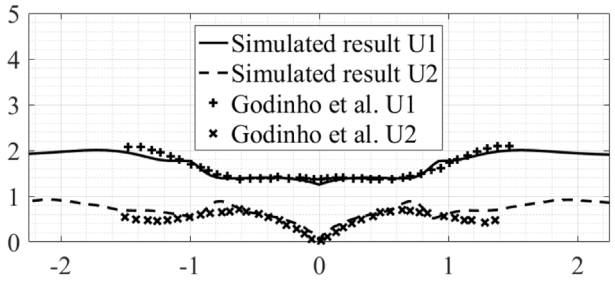

Fig. 5. Comparison of simulation results with the corresponding results of Godinho et al. [30].

stress concentrations and large deformations. Then, the SH wave with displacement equation $u(t) = sin(\frac{2\pi}{0.3})t$ is input vertically to the model from the bottom boundary.

The peak values of displacement inspired by the input signal are recorded at the monitoring points on the free surface, as shown in Fig. 4(D). According to the responses of the validation model, a comparison between records at monitoring points and the analytical results of Godinho et al. [30] indicates the excellent reliability of the methods used, shown in Fig. 5. Thus, the introduction of viscoelastic boundary and equivalent nodal load can effectively reflect the propagation characteristics of seismic signals.

2.2. 3D numerical modeling for irregular topography

The time spent on modeling and meshing far exceeds the time spent on calculations and data analysis [27]. During our study, for modeling and meshing 3D terrain, a convenient way that integrates SketchUp, SolidWorks and Abaqus is proposed. Voxelization is well-suited for fine surface generation and is widely used, where the octree method involves computational processes such as octree traversal, neighborhood search and interpolation operations. These place a very high demand on computational resources [49]. Fine-grained generation of topography is not required in this study. Broader data sources and more efficient terrain generation methods are targeted. Triangulating point clouds is an intuitive and intuitive method for effectively approximating complex surfaces by connecting adjacent points to form triangles. Some triangulation algorithms, especially the Delaunay triangulation algorithm, have good computational efficiency and can generate high-quality meshes in a relatively short period. As an efficient method, triangularization converts the point cloud to the surface model, but the triangularization makes the surface model completely segmented. The sizes and shapes of the triangular grids are less regular, especially on the more complex terrain. As a result, the shapes of the surface grids make it impossible to automatically generate hexahedral elements when meshing. Although the element division can be performed by more tetrahedral elements, the dramatic increase in the number of elements will demand more computational resources and consume more time, which is inefficient in practice. Besides, the severe irregularity of the triangular grid causes the element division and quality control near the surface to be more complex, and the program's design for artificial boundary and signal input is also a challenge. A complete surface can minimize the influence caused by triangular grids on the generation of hexahedral elements. Using the topology tool for surfaces allows the divided meshes after triangulation to be processed into a whole. This will simplify the overall process of modeling. This is because the processing of the model will no longer be affected by the severed surfaces.

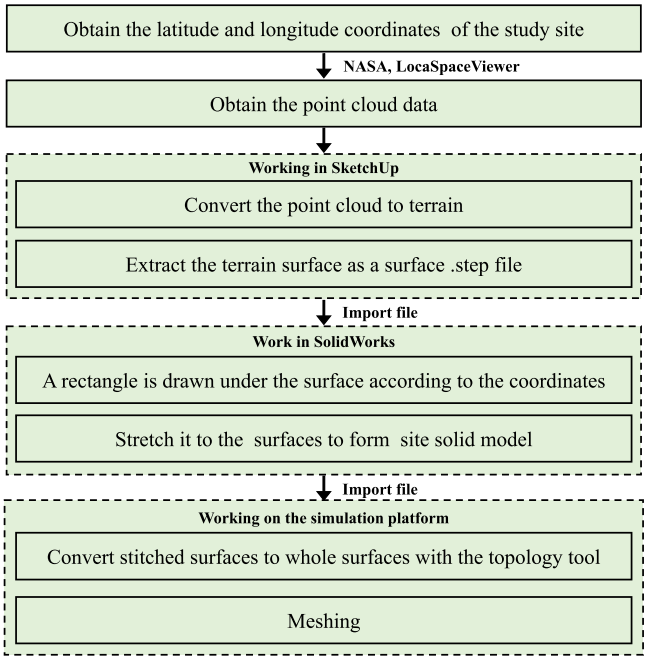

Fig. 6. 3D modeling flowchart.

Modeling the site plays a crucial role in geotechnical engineering study. As a consequence, an analysis procedure is summarized in Fig. 6 for saving time in numerical simulation. Solving the displacement equation is the key step of FEM. The system of equations for this step is usually expressed as $KU = F$, where K is the stiffness matrix, U is the unknown displacement vector, and F is the external load vector, the size of K is proportional to the square of the number of elements, the size of U is proportional to the number of nodes. The time complexity of the computation is very closely related to the number of elements and nodes. The hexahedron will consist of at least 4 tetrahedra without an increase in the number of nodes. Therefore if the hexahedron in the original model is represented by a minimum of tetrahedra, it will make the number of elements at least 4 times as large. The time complexity of the computation would be 16 times that of the hexahedral element scheme. However, the fact that the number of tetrahedral elements will be more than four times that of the original hexahedral elements, and the number of nodes will need to be increased to ensure that the dimensions of the longest edges of the elements will still comply with the requirements of Eq. (4). It means that the use of tetrahedral elements will result in the time complexity of solving the system of equations will be more than 16 times of the original scheme.

2.3. Case study

Within the research region, the combination of climate and altitude makes the region the origin of many rivers in Asia. The downcutting of rivers and geological tectonic movements have created many valleys in South-west China [42]. Complex topography and high seismic risk bring importance to seismic damage analysis in river valleys. As a result, a typical river valley site in South-west China with more than a 1000 m drop is chosen for the case study. A national trunk highway, located next to the river and nearing the valley's bottom, traverses the study area. The topographical characteristics and regional situation are

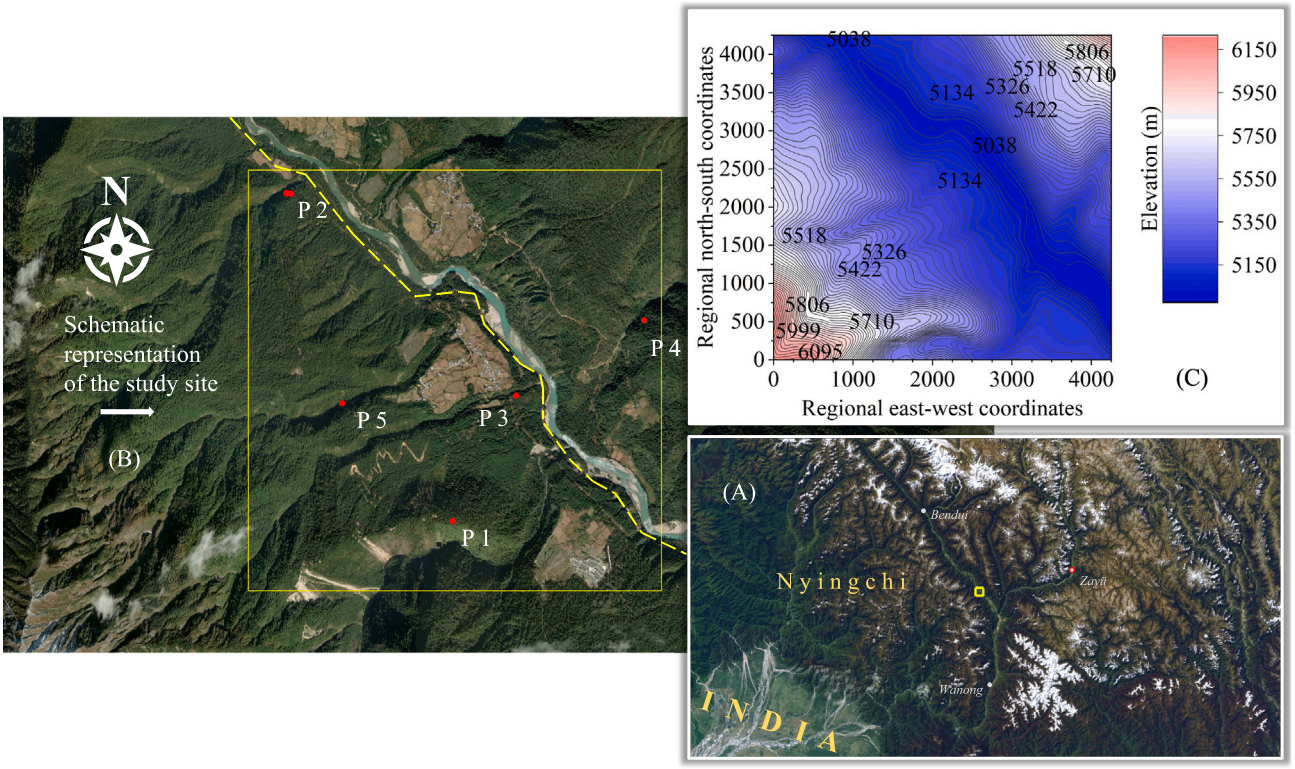

Fig. 7. Regional environment and its contour map. (A) An overhead view of the Plateau canyon landscape where the study area is located, showing the study site's location, (B) The canyon where the river is located and the points P1 to P5 that will be studied subsequently (yellow dashed line is the highway), (C) Contour map of the study region. (For interpretation of the references to color in this figure legend, the reader is referred to the web version of this article.)

indicated in Figs. 1 and 7(A). The road is located next to the river, nearing the bottom of the canyon. The regional environment in which the site is located and its contours are indicated in Fig. 7.

2.3.1. Site 3D finite element model

As shown in Fig. 8(A), the 3D terrain model of the study area is established by point cloud, which is obtained from LocaSpaceViewer. The generation process is described in Section 2.2, and the 3D site model and the element division result are shown in Fig. 8(B). 249 278 elements (C3D8R) were used to form the site model with horizontal dimensions of 4250 meters by 4250 m.

Site amplification factor is dependent on site conditions, including topography and properties of rock and soil. A single material is employed for the study to focus on seismic signals and site topography. The rock is considered linear elastic, and the material parameters of the model are as follows: $\rho = 2200\ \mathrm{kg/m^3}$, modulus of elasticity $E = 9.36 \times 10^9$ Pa, Poisson's ratio $\nu = 0.25$; shear wave velocity $C_S = 1200$ m/s. The nonlinear properties of rocks and overlying soil have significant impacts on seismic response analysis [25]. Moreover, they may interact with topographic effects. While considering both aspects could enhance the reliability of the results, it would also introduce additional complexity. Therefore, to focus on the primary objective, the elastic materials are applied in this study to explore the effects of tomographic irregularities and excitation frequency on seismic site amplification.

2.3.2. Input excitation

(1) Artificial signals

SH waves incident vertically from the model bottom. The input seismic signals use pulse-like waveforms. The pulse waves are generated by finite difference of the δ function shown as Eq. (5) [46].

$$F(\tau) = 16[G_4(\tau) - 4G_4\left(\tau - \frac{1}{4}\right) + 6G_4\left(\tau - \frac{1}{2}\right) - 4G_4\left(\tau - \frac{3}{4}\right) + G_4(\tau - 1)] \tag{5}$$

where $G_4(\tau) = \tau^3 H(\tau)$, $\tau = \frac{t}{T}$, T is the pulse holding time, $H(\tau)$ is the Heaviside function. Set the pulse holding time as 1 s, 0.5 s, 0.$\dot{3}$ s, 0.25 s, 0.2 s. The waveform is shown in Fig. 9. According to the displacement pulse, the equivalent nodal load calculation is performed in the way in 3.2. The seismic load is input afterward.

(2) Seismic records

Sixteen seismic records are selected for input as actual seismic signals. The seismic responses of the actual signals are compared with those of artificial signals to verify the universality of the results. The seismic records are from Chi-Chi, Taiwan earthquake in PEER NGA-Weat2 database. The earthquake magnitude and hypocenter depth of the earthquake are 7.62 Mw and 8 km, respectively. Sixteen seismic ground motions are adopted as input excitations, and information on these ground motions is listed in Table 2. The time curves and Fourier spectrum of acceleration, velocity and displacement for the first seismic records are shown in Fig. 9. The time curves and Fourier spectral information for the remaining fifteen signals are in the Supporting Information.

3. Results

3.1. Distribution of peak amplification factors of motion parameters

The topographic amplification effect can be analyzed after applying the above seismic signal. The seismic responses are investigated through the extraction of surface nodal accelerations, velocities and displacements. The spatial distribution of peak values of motion parameters amplification is depicted to consider the relationship between seismic response and topographic characteristics. Figs. 10–12 show the features of spatial variability.

As shown in Fig. 10, the significant amplification area coinciding with the ridges can be observed in the acceleration results when signal frequencies are under 4 Hz. The contrast of seismic responses between

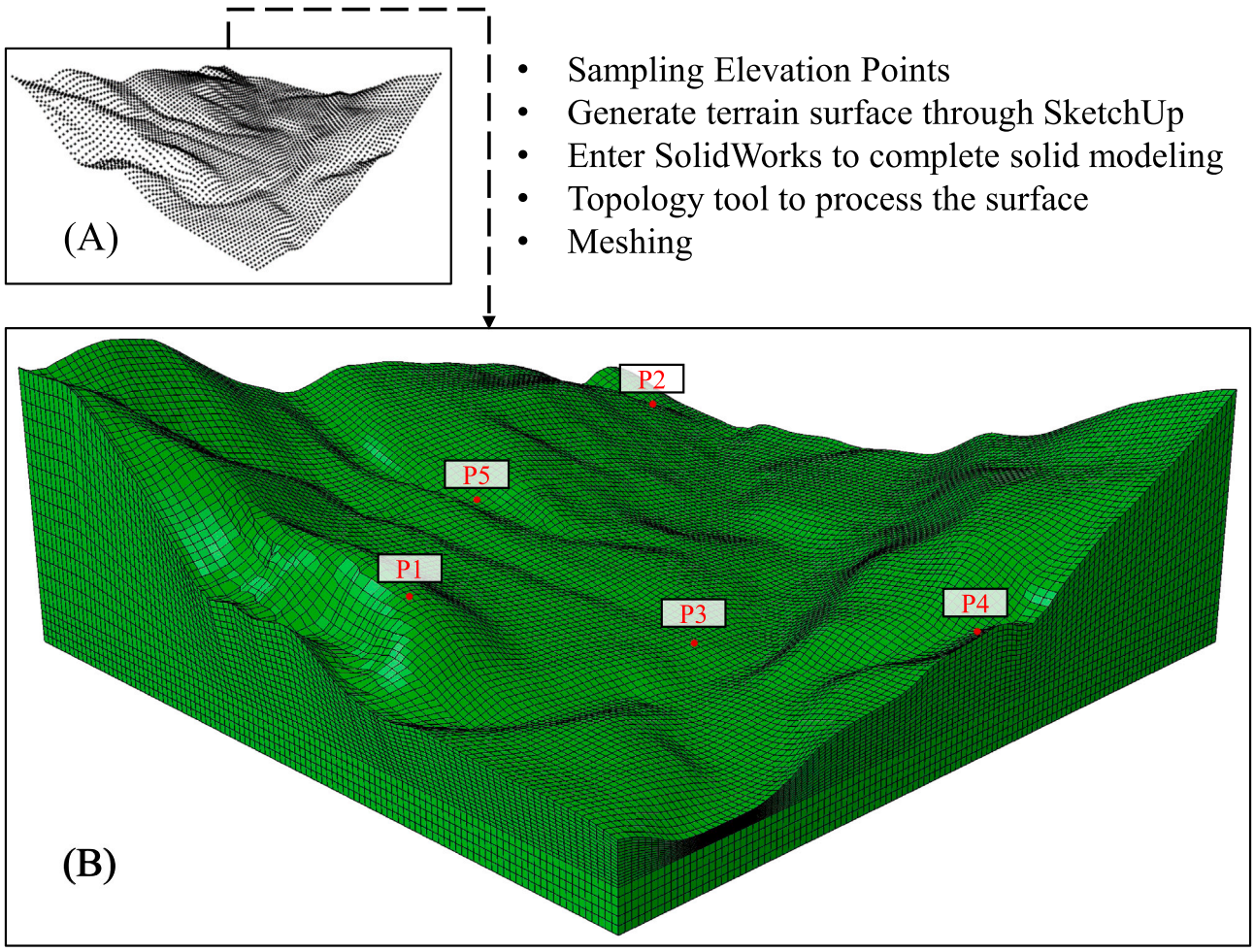

Fig. 8. Point cloud generation topography and meshing. (A) Result of spatialization of the point cloud in SketchUp, (B) Finite element model after modeling and meshing.

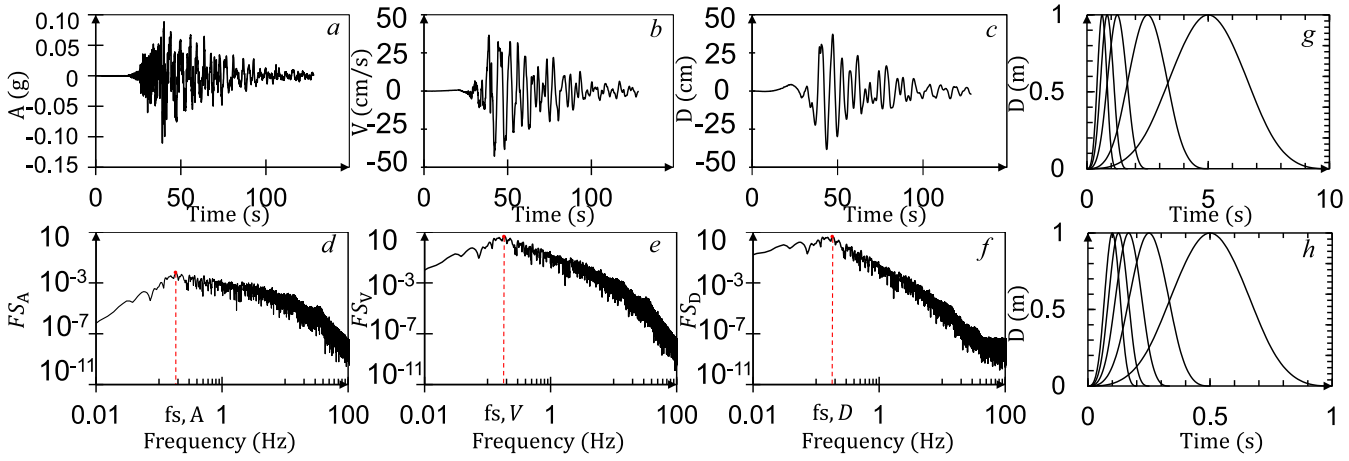

Fig. 9. Input excitation for seismic site response, where FS_A is the Fourier spectra of acceleration, FS_V is the Fourier spectra of velocity, FS_D is the Fourier spectra of displacement, fs_A is the dominant frequency of acceleration, fs_V is the dominant frequency of velocity, fs_D is the dominant frequency of displacement. (a)–(f) The time curves and Fourier spectra of acceleration, velocity and displacement of the No. 1 ground motion in Table 2, (g) The artificial signals of 0.1, 0.2, 0.4, 0.6 and 0.8 Hz, (h) The artificial signals of 1, 2, 3, 4 and 5 Hz.

the ridge line and the ravine line is obvious. The acceleration response in the support material all showed similar results. Besides, when the input signal frequency is high, seismic response strength is lower than low-frequency signal results. However, some of the ravine areas show unexpected amplification with the rising signal frequencies, even more significant than adjacent ridges, shown in Fig. 10(B). This phenomenon is also detected in the velocity results. Only the corresponding phenomenon in the acceleration results is labeled because it is more pronounced in the acceleration results. The observation phenomenon is inconsistent with the traditional assertion that concave topography decreases seismic response [50]. This phenomenon is also mentioned by Gao et al. [51] during an investigation of an analytical U-shaped

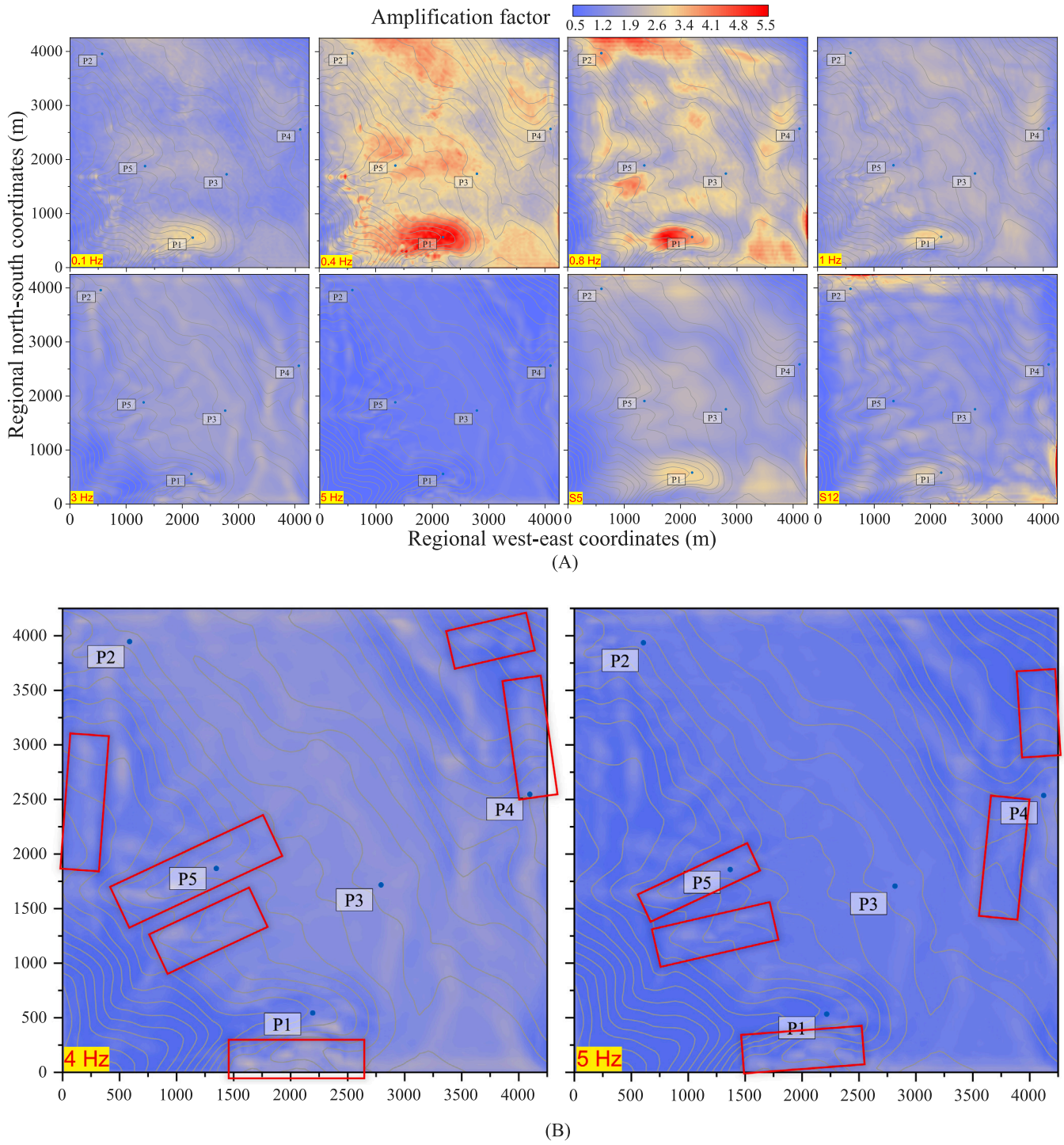

Fig. 10. Distribution of peak acceleration amplification factors on the terrain surface. The distribution under signals with 0.1 Hz, 0.4 Hz, 0.8 Hz, 1 Hz, 3 Hz, 5 Hz, No. 5 and No. 12 seismic records(S5 and S12) in Table 2, (B) The distribution with 4 Hz and 5 Hz input signals, inside the red squares are some of the ravines where amplification occurs.

valley model. A similar unexpected phenomenon may be relevant to the signal frequency. According to the information in Table 2, the only records with acceleration dominant frequencies close to or above 4 Hz are Record 4 and Record 8, whose response results can be viewed in the additional material. However, these two records show the same spatial response pattern to the artificial signals results under 4 Hz, which means that the dominant frequency cannot be used as a complete judgment of spatial response pattern.

Velocity amplification factor spatial distributions indicate a regularity similar to the acceleration amplification factor as shown in Fig. 11. In comparison, under the artificial signals excitation, response results of velocity show greater amplification than acceleration results. In contrast, the velocity response results caused by the actual signal are not significant compared with the acceleration responses. Additionally, the amplification at the ravine area shown in acceleration responses has not been found as the increasing of input signal frequencies. Similarly, the seismic response strengths of different signal frequencies show the same pattern as the above investigation about acceleration with the signal frequencies under 4 Hz. Besides, a non-monotonic correlation is shown between the response result and the input frequency.

Table 2
Information of selected ground motions from Chi-Chi, Taiwan earthquake.

No.	RSN	Direction	Station name	Hypercenter distance (km)	Joyner–Boore distance (km)	$V_{S,30}$ (m/s)	$f_{s,A}$	$f_{s,V}$	$f_{s,D}$
1	1180	H2	CHY002	44.69	24.96	235.13	0.19	0.19	0.19
2	1181	H2	CHY004	72.07	47.32	271.30	0.16	0.16	0.16
3	1236	H1	CHY088	69.24	37.48	318.52	0.49	0.49	0.05
4	1281	H1	HWA032	62.75	42.87	573.04	3.78	0.73	0.73
5	1964	H1	KAU032	150.08	111.02	194.13	0.60	0.37	0.37
6	1372	H1	KAU043	215.62	170.99	538.49	0.37	0.37	0.03
7	1397	H1	KAU086	129.32	95.87	216.80	0.28	0.18	0.11
8	1404	H1	PNG	132.90	110.30	465.86	8.37	0.42	0.42
9	1406	H2	SSD	124.60	83.38	535.13	2.39	0.56	0.32
10	1429	H1	TAP041	160.36	110.28	363.56	0.43	0.11	0.07
11	1482	H1	TCU039	71.95	19.89	540.66	0.13	0.13	0.13
12	1495	H1	TCU055	36.74	6.34	359.13	0.87	0.35	0.31
13	1499	H2	TCU060	46.07	8.51	375.42	0.17	0.11	0.10
14	1500	H1	TCU061	42.81	17.17	379.64	0.31	0.13	0.13
15	1509	H1	TCU074	20.69	0	549.43	1.07	0.38	0.12
16	1537	H1	TCU111	45.50	22.12	237.30	0.27	0.27	0.03

RSN is the Record Sequence Number in PEER NGA-West2 flatfile; H1 and H2 are the horizontal 1 and horizontal 2 direction in the flatfile, respectively; $V_{s,30}$ is shear Wave Velocity (Vs) averaged over a depth of 30 meters near the earth's surface, $f_{s,A}/f_{s,V}/f_{s,D}$ is dominant frequency on acceleration, velocity, displacement of seismic record, respectively.

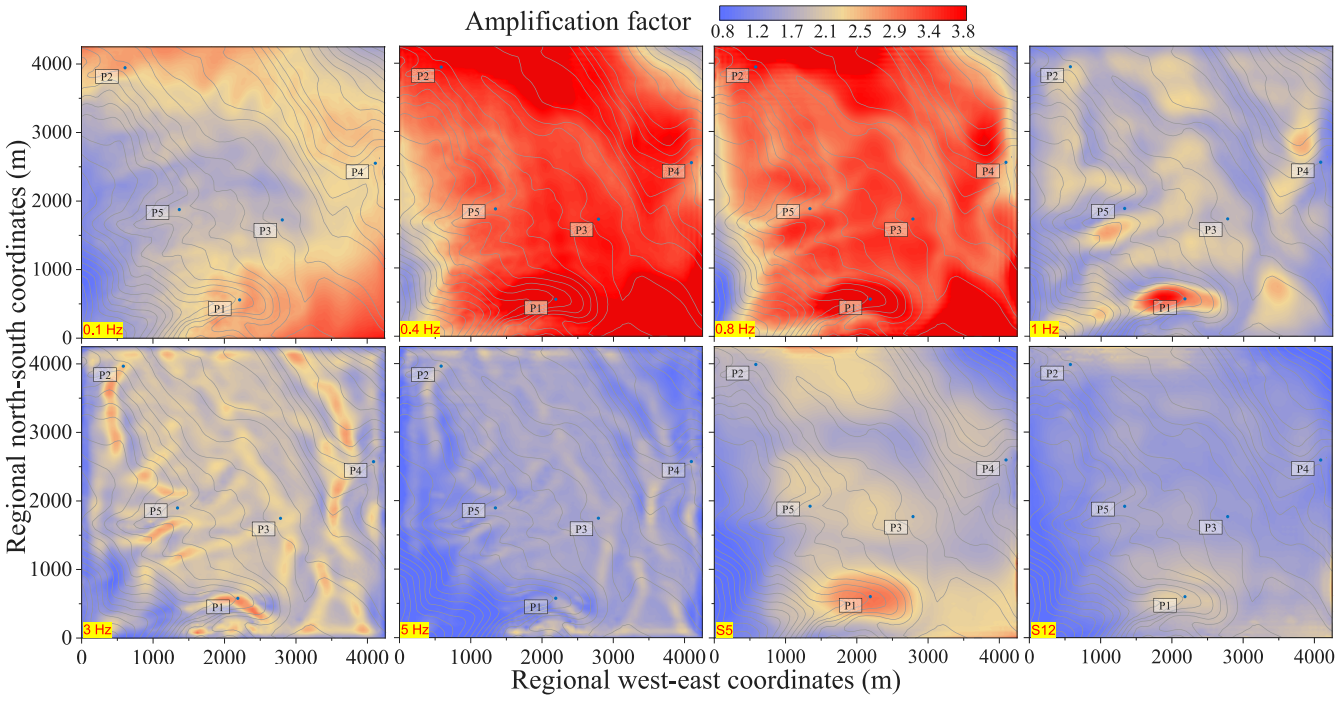

Fig. 11. Distribution of peak velocity amplification factors on the terrain surface. The distribution under signals with 0.1 Hz, 0.4 Hz, 0.8 Hz, 1 Hz, 3 Hz, 5 Hz, No. 5 and No. 12 seismic records(S5 and S12) in Table 2.

The displacement amplification factor distributions of the artificial and actual signals show weaker spatial variability and lower degrees of topographic amplification effect than both acceleration and velocity as shown in Fig. 12. The spatial distribution of displacement amplification factors is also similar to the velocity and acceleration except for 4 Hz and above. The same as velocity responses, the displacement responses show a trend that the response strengths rise initially and then fall with the increasing input signal frequencies. Weaker spatial correlations are shown in the response results with respect to the actual seismic record, see the Support Information for details.

3.2. Correlation of points' amplification factor with frequency

As shown in Fig. 7(B). Based on the above investigation, the motion parameters all show spatial properties related to the topography. Moreover, the investigation reveals possible patterns between response strength and input signal frequency. Several points located at ravines and ridges are selected near the road, with excellent engineering significance. The points are numbered from P1 to P5, where P1 is located on a typical ridge, P2 and P3 are located on gentler ridges, while P5 is located in gentler ravines and P4 is located in typical ravines.

Fig. 13 illustrates the displacement responses at P1 to P5 under various signal frequency and seismic records excitations. At points P1, P2 and P3, the response strengths of ground motion are significantly higher than those at points P4 and P5. Considering the terrain of each point located, the difference between points at ravines and ridges can be linked to previous analyses of inconsistent seismic responses. P1, P2, and P3, as measurement points on the ridge, all present higher amplification factor (α) compared to P4 and P5 in the ravine, which matches the results in Figs. 10–12. The results of the analysis for the selected points have consistent results with the amplification factor spatial distribution, i.e., ridges lead to a greater amplification effect

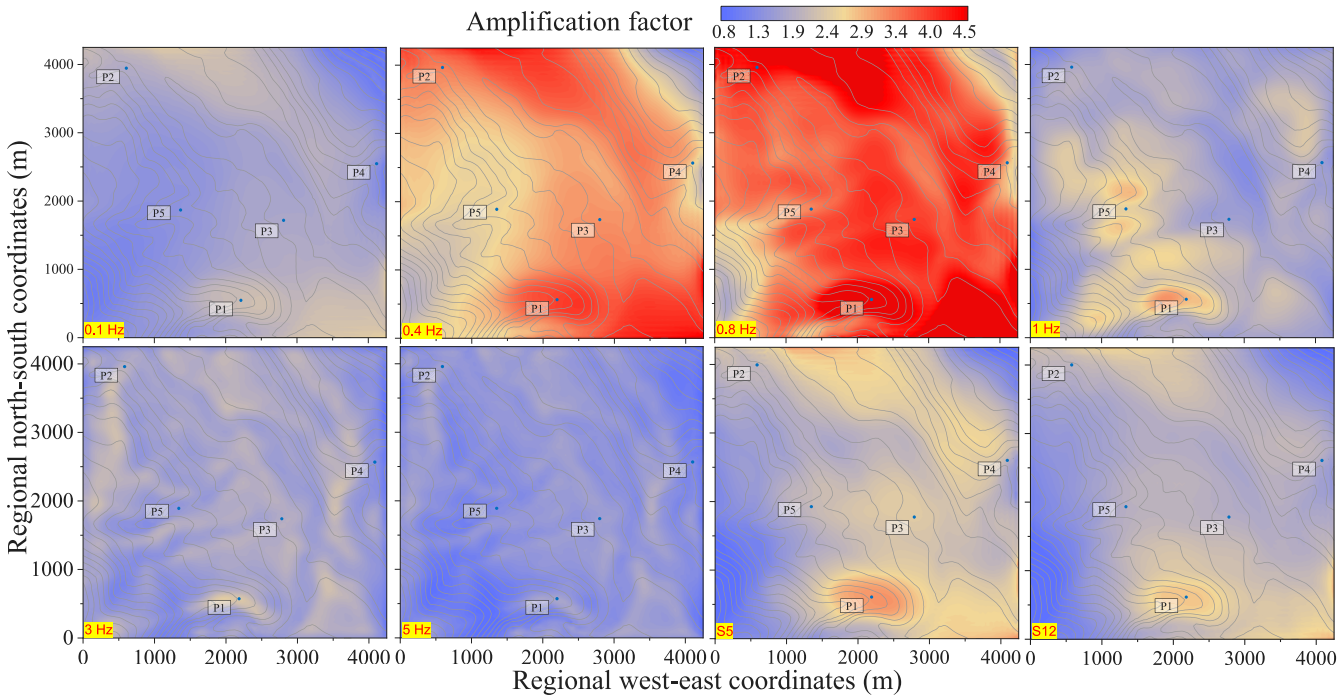

Fig. 12. Distribution of peak displacement amplification factors on the terrain surface. The distribution under signals with 0.1 Hz, 0.4 Hz, 0.8 Hz, 1 Hz, 3 Hz, 5 Hz, No. 5 and No. 12 seismic records(S5 and S12) in Table 2.

compared to ravines. Further, we examined the response intensity of the whole research area, focusing on the statistical characterization parameters of the amplification factor. Results similar to Fig. 13 are obtained (see Fig. 14). The response intensities of the sites also show high levels below 1 Hz and peak intensities of acceleration, velocity, and displacement around 0.4, 0.6, and 0.8, respectively.

Additionally, for the presented model, the resonance frequency (T_0) is 0.3415 Hz. Based on Fig. 13, the α is higher for both artificial signals and seismic records when the frequency of the input signal (dominant frequency for seismic record) is lower than 1 Hz. The α for both artificial signals and seismic records reaches a maximum near T_0 and the α for seismic records tend to be smaller compared to artificial signal response results. Besides, a similar trend of variation of the response intensity is presented in the frequency (dominant frequency for seismic record) range of 0.1–5 Hz at the observed points.

Based on Eurocode8 [52], the response results were compared with the recommended topographic amplification factor S. According to Fig. 13, when the dominant frequency of the actual seismic record is close to the resonance frequency of the site model, the site amplification factor far exceeds the recommended value. It even reaches more than 2 times at point P1, the typical raised terrain on the site model.

4. Discussions

The amplification of seismic site responses in ridge areas has been extensively explored in previous studies [53]. In this study, we examine the effects of input signal frequency, revealing that the site amplification can statistically differ by a factor of two when various frequency signals are input into the model. This phenomenon may be related to the terrain span. The most significant amplification occurs with signal wavelengths close to the span the terrain, explaining the intensity variation with different signal frequencies [17].

In addition, some unexpected amplifications are found at ravine areas under the input signal frequencies over 4 Hz. A similar phenomenon is mentioned by Gao et al. [51], with an unusual amplification of the bottom of the U-shaped valley. Gao et al. [51] also present that the U-shaped valley bottom amplification factors correlate with input signal wavelengths. The general qualitative conclusion that convex terrain shows a more significant seismic response is not strictly available. Thus the following inference is made: because adjacent ridges and ravines may have different dimensions, the wavelengths for their most significant response differ. Higher intensity response may appear at the ravine area when the input signal wavelength is close to the size of the ravine rather than the adjacent ridge. Consequently, the unexpected ravine amplification appears at specific input signal frequencies.

5. Conclusions

This study focuses on the effects of topographic irregularities on seismic site amplification. To comprehensively understand the relationship between seismic response and topographic characteristics of the entire site, we proposed a novel analysis procedure for 3D actual site modeling and meshing. Viscoelastic boundary and equivalent nodal force are integrated to conduct finite element simulation of seismic wave propagation. The effectiveness of the method is also validated. Furthermore, the relationship between the ground motion frequency and topographic characteristics is investigated. The main conclusions are derived as follows.

(1) The relationship between topographic characteristics and seismic response is elucidated by analyzing the seismic response at the actual valley site. The spatial distribution of the peak value of seismic response is found to be closely related to the topographic features, with significantly amplified areas largely coinciding with the ridge areas in most cases. However, ravine areas show amplification when input signal frequencies are above 4 Hz, which is not consistent with the classical view that concave terrain decreases seismic response intensity. Noticeable differences in seismic response are observed when comparing ridge areas with ravine areas.

(2) The seismic site amplification is significantly influenced by the excitation frequency and is closely tied to the fundamental period of the site. While the amplification value varies at different points due to tomographic irregularities, the trend of site amplification caused by frequency remains consistent. Specifically, the intensity of seismic site amplification rises with the input signal frequency, reaching its

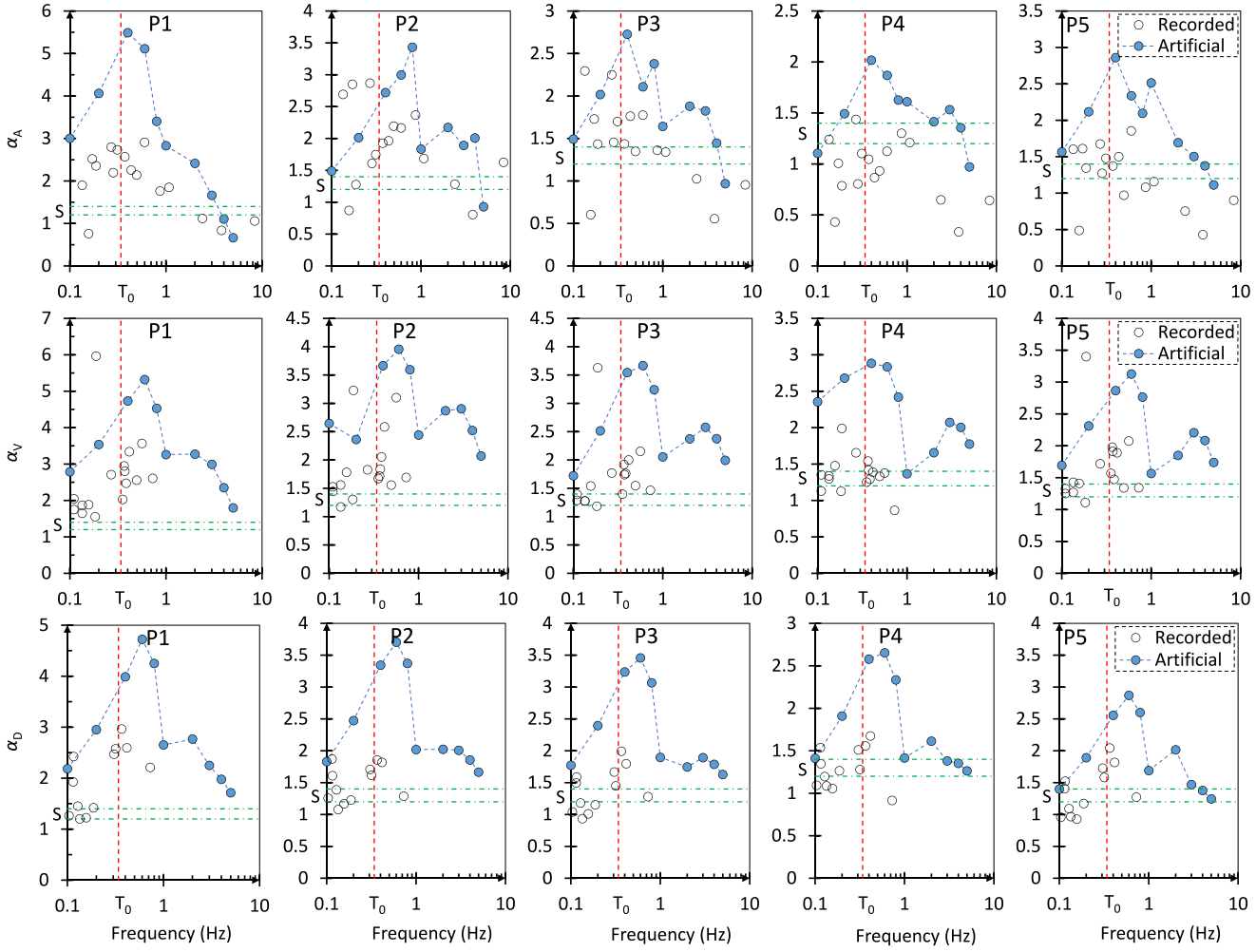

Fig. 13. Amplification factors (α) of P1–P5 with respect to the frequency of input excitation (the dominant frequency is used for actual seismic records). α_A is the amplification factor of the acceleration, α_V is the amplification factor of the velocity, α_D is the amplification factor of the displacement. T_0 is the resonance frequency of the site model. S is the recommended topography amplification factor mentioned in Eurocode8, 1.4 for the upper and 1.2 for the lower.

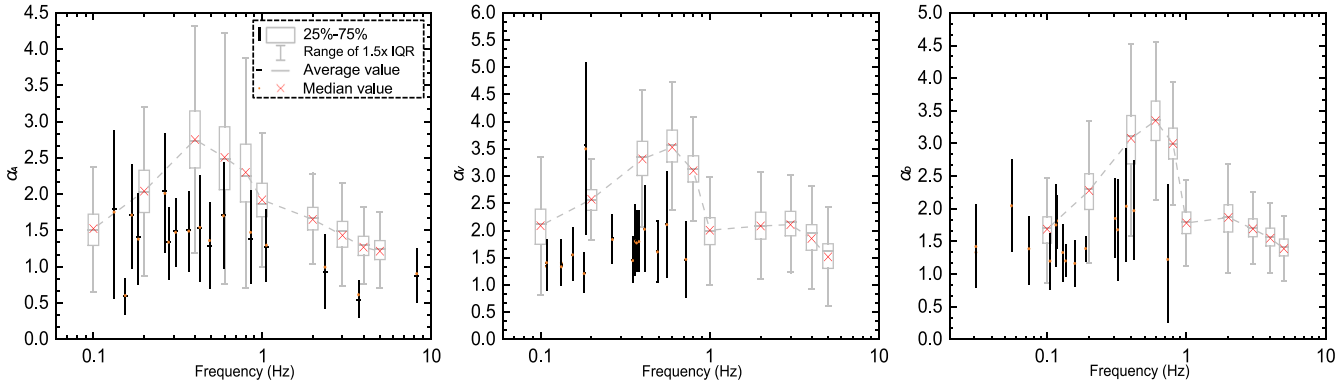

Fig. 14. Boxplot about the amplification factor (α) of all surface points with respect to the input excitation (dominant frequency is used for the actual seismic records). α_A is the amplification factor for acceleration, α_V is the amplification factor for velocity, and α_D is the amplification factor for displacement. IQR is the Inter-Quartile Range.

peak value around the fundamental period of the site. Subsequently, it decreases as the input signal frequency consistently increases. This consistent pattern holds true when the sites are statistically examined as a whole, applicable to both artificial waves and actual seismic records. This observation may offer a valuable reference for the rapid assessment of seismic site amplification effects.

(3) The simulation results of this study reach more than two times the recommended value of the Eurocode8 topographic amplification factor at the examined points. The results of several actual seismic records are above the recommended value of Eurocode8. This implies that the standard may require further examination of the topographic magnification factor in combination with soil characteristics, etc., to avoid underestimating the damage of earthquakes.

This work sheds new insight into regional seismic risk analysis with the developed numerical method for 3D real sites. The varying seismic site responses between ravines and ridges underscore the potential

for severe structural damage when topographic irregularities are not taken into account. Secondary disasters can also be led by inconsistent response during seismic propagation. Therefore, this study has developed a valuable tool to enhance our understanding of seismic site amplification, which could aid in seismic design and risk analysis.

CRediT authorship contribution statement

Zhe-Xing Chen: Writing – review & editing, Writing – original draft, Visualization, Validation, Methodology, Data curation. **Guan Chen:** Writing – review & editing, Writing – original draft, Visualization, Methodology, Investigation, Funding acquisition, Conceptualization. **Yong Liu:** Writing – review & editing, Supervision, Project administration, Funding acquisition.

Declaration of competing interest

The authors declare that they have no known competing financial interests or personal relationships that could have appeared to influence the work reported in this paper.

Data availability

Data will be made available on request.

Acknowledgments

This research is supported by the National Natural Science Foundation of China (Grant No. U22A20596) and the Natural Science Foundation Innovation Group Project of Hubei Province, China (Grant No. 2023AFA017). Guan Chen would like to thank the financial support of Sino-German (CSC-DAAD) Postdoc Scholarship Program.

Appendix A. Supplementary data

Supplementary material related to this article can be found online at https://doi.org/10.1016/j.engstruct.2024.117667.

References

[1] Yao Y, Wang R, Liu T-Y, Zhang J-M. Seismic response of high concrete face rockfill dams subjected to non-uniform input motion. Acta Geotech 2022;14(1):83–100.
[2] Asano K, Iwata T. Source rupture processes of the foreshock and mainshock in the 2016 Kumamoto earthquake sequence estimated from the kinematic waveform inversion of strong motion data. Earth Planets Space 2016;68:147.
[3] Maugeri M, Simonelli AL, Ferraro A, Grasso S, Penna A. Recorded ground motion and site effects evaluation for the april 6 2009l'aquila earthquake. Bull Earthq Eng 2011;9(1):157–79.
[4] Kubo H, Iwaki A, Suzuki W, Aoi S, Sekiguchi H. Estimation of the source process and forward simulation of long-period ground motion of the 2018 Hokkaido Eastern Iburi, Japan earthquake. Earth Planets Space 2019;71(1):98.
[5] Rathje EM, Kottke AR, Trent WL. Influence of input motion and site property variabilities on seismic site response analysis. J Geotech Geoenviron Eng 2010;136(4):607–19.
[6] Gautam D, Forte G, Rodrigues H. Site effects and associated structural damage analysis in Kathmandu Valley, Nepal. Earthq Struct 2016;10(5):1013–32.
[7] Papaspiliou M, Kontoe S, Bommer JJ. An exploration of incorporating site response into PSHA-Part I: Issues related to site response analysis methods. Soil Dyn Earthq Eng 2012;42:302–15.
[8] Manandhar S, Cho HI, Kim DS. Effect of bedrock stiffness and thickness of weathered rock on response spectrum in Korea. KSCE J Civ Eng 2016;20(7):2677–91.
[9] Sengupta S, Sarkar R, Kolathayar S, Drukpa D. Deterministic seismic hazard analysis for Phuentsholing region of southern Bhutan considering local site effects. Innov Infrastruct Solut 2022;7(6):361.
[10] Chaudhary MTA. A study on sensitivity of seismic site amplification factors to site conditions for bridges. Bull N Z Soc Earthq Eng 2018;51(4):197–211.
[11] Pitilakis K, Riga E, Anastasiadis A. New code site classification, amplification factors and normalized response spectra based on a worldwide ground-motion database. Bull Earthq Eng 2013;11(4):925–66.
[12] Pitilakis K, Riga E, Anastasiadis A, Fotopoulou S, Karafagka S. Towards the revision of EC8: Proposal for an alternative site classification scheme and associated intensity dependent spectral amplification factors. Soil Dyn Earthq Eng 2019;126:105137.
[13] Paolucci R, Aimar M, Ciancimino A, Dotti M, Foti S. Checking the site categorization criteria and amplification factors of the 2021 draft of Eurocode 8 Part 1–1. Bull Earthq Eng 2021;19(11):4199–234.
[14] Durante MG, Brandenberg SJ, Ausilio E, Zimmaro P. On the combined effect of topographic irregularities and wave passage on the spatial variation of seismic ground motion. Bull Earthq Eng 2022;20(7):3577–92.
[15] Liu Z-X, Li W-X, Jin L-G, Meng S-B, Yuan X-M, Cheng X-L, Ai T-C. Efficient simulation of stochastic seismic response of long-span bridges in river valleys using hybrid BEM-FEM. Soil Dyn Earthq Eng 2023;165:107690.
[16] Liang J-W, Wu M-T, Ba Z-N. Simulating elastic wave propagation in 3-D layered transversely isotropic half-space using a special IBEM: Hill topography as an example. Eng Anal Bound Elem 2021;124(1):64–81.
[17] Paolucci R. Amplification of earthquake ground motion by steep topographic irregularities. Earthq Eng Struct Dyn 2002;31(10):1831–53.
[18] Jeong S, Asimaki D, Dafni J, Wartman J. How topography-dependent are topographic effects? Complementary numerical modeling of centrifuge experiments. Soil Dyn Earthq Eng 2019;116:654–67.
[19] Muñoz A, Sáez E. Numerical estimation of site effects in the city of Arica due to natural soil variability using the spectral elements method. Bull Earthq Eng 2018;16(1):459–78.
[20] Pasqua FD, Benites R, Massey C, MacSaveney M. Numerical evaluation of 2D versus 3D simulations for seismic slope stability. In: Advancing culture of living with landslides.. 2017, p. 557–64, 4th World Landslide Forum.
[21] Makra K, Chávez-García FJ. Site effects in 3D basins using 1D and 2D models: an evaluation of the differences based on simulations of the seismic response of Euroseistest. Bull Earthq Eng 2016;14(4):1177–94.
[22] Narayan JP, Sahar D. Three-dimensional viscoelastic finite-difference code and modelling of basement focusing effects on ground motion characteristics. Comput Geosci 2014;18(6):1023–47.
[23] Yousefi-Bavil K, Koçkar MK, Akgün H. Development of a three-dimensional basin model to evaluate the site effects in the tectonically active near-fault region of Gölyaka basin, Düzce, Turkey. Nat Hazards 2022;114(1):941–69.
[24] Ozaslan B, Iyisan R, Hasal ME, Khanbabazadeh H, Yamanaka H. Assessment of the design spectrum with aggravation factors by 2D nonlinear numerical analyses: a case study in the Gemlik Basin, Turkey . Bull Earthq Eng 2022;20(3):1371–95.
[25] Huang D-R, Sun P-G, Jin F, Du C-Y. Topographic amplification of ground motions incorporating uncertainty in subsurface soils with extensive geological borehole data. Soil Dyn Earthq Eng 2021;141:106441.
[26] Liang J-W, Wu M-T, Ba Z-N. Simulating elastic wave propagation in 3-D layered transversely isotropic half-space using a special IBEM: Hill topography as an example. Eng Anal Bound Elem 2021;124:64–81.
[27] Tiwari RC, Bhandary NP. 3D SEM-based seismic ground response analysis of Kathmandu Valley in 2015 Gorkha Nepal earthquake. J Seismol 2021;25(5):1321–38.
[28] Soltani N, Javdanian H, Soltani N. Assessing the interaction of seismically loaded adjacent valleys using time-domain approach. Acta Geod Geophys 2021;56(1):133–44.
[29] Liu Z-X, Qiao Y-F, Cheng X-L, El Naggar MH. Nonlinear seismic response and amplification effect of 3D sedimentary basin based on bounding surface constitutive model. Soil Dyn Earthq Eng 2022;158:107292.
[30] Godinho L, Amado Mendes P, Tadeu A, Cadena-Isaza A, Smerzini C, Sanchez-Sesma FJ, Madec R, Komatitsch D. Numerical simulation of ground rotations along 2D topographical profiles under the incidence of elastic plane waves. Bull Seismol Soc Am 2009;99(2B):1147–61.
[31] Nguyen K-V, Gatmiri B. Evaluation of seismic ground motion induced by topographic irregularity. Soil Dyn Earthq Eng 2007;27(2):183–8.
[32] Chen Z-W, Huang D-R, Wang G. Large-scale ground motion simulation of the 2016 Kumamoto earthquake incorporating soil nonlinearity and topographic effects. Earthq Eng Struct Dyn 2022;52(4):956–78.
[33] Panzera F, Alber J, Imperatori W, Bergamo P, Fäh D. Reconstructing a 3D model from geophysical data for local amplification modelling: The study case of the upper Rhone valley, Switzerland. Soil Dyn Earthq Eng 2022;155:107163.
[34] Li J-B, Zhou L, Li S-Y, Lin G, Ding Z-X. Soil-structure interaction analysis of nuclear power plant considering three-dimensional surface topographic irregularities based on automatic octree mesh. Eng Struct 2023;275:115161.
[35] Restrepo D, Bielak J, Serrano R, Gómez J, Jaramillo J. Effects of realistic topography on the ground motion of the Colombian Andes - A case study at the Aburra Valley, Antioquia. Geophys J Int 2016;204(3):1801–16.
[36] Semblat J, Dangla P, Kham M, Duval A. Seismic site effects for shallow and deep alluvial basins: in-depth motion and focusing effect. Soil Dyn Earthq Eng 2002;22(9–12):849–54.
[37] Kim S, Ohtake Y, Nagai Y, Suzuki H. A novel interpolation scheme for dual marching cubes on octree volume fraction data. Comput Graph-UK 2017;66(SI):169–78.

[38] Botsch M, Sorkine O. On linear variational surface deformation methods. IEEE Trans Vis Comput Graph 2008;14(1):213–30.
[39] Jia G, Wang X, Wei H. An effective approach for selection of terrain modeling methods. IEEE Geosci Remote Sens Lett 2013;10(4):875–9.
[40] Zhao B, Su L-J, Xu Q, Li W-L, Xu C, Wang Y-S. A review of recent earthquake-induced landslides on the Tibetan Plateau. Earth-Sci Rev 2023;244:104534.
[41] Harrison TM, Copeland P, Kidd WS, Yin A. Raising tibet. Science 1992;255(5052):1663–70.
[42] Yang K, Wu H, Qin J, Lin C-G, Tang W-J, Chen Y-Y. Recent climate changes over the Tibetan Plateau and their impacts on energy and water cycle: A review. Glob Planet Change 2014;112:79–91.
[43] You Q-L, Chen D-L, Wu F-Y, Pepin N, Cai Z-Y, Ahrens B, Jiang Z-H, Wu Z-W, Kang S-C, AghaKouchak A. Elevation dependent warming over the Tibetan Plateau: Patterns, mechanisms and perspectives. Earth-Sci Rev 2020;210:103349.
[44] Cui P, Ge Y-G, Li S-J, Li Z-H, Xu X-W, Zhou GGD, Chen H-Y, Wang H, Lei Y, Zhou L-B, Yi S-J, Wu C-H, Guo J, Wang Q, Lan H-X, Ding M-T, Ren J-J, Zeng L, Jiang Y-J, Wang Y. Scientific challenges in disaster risk reduction for the Sichuan-Tibet Railway. Eng Geol 2022;309:106837.
[45] Deeks AJ, Randolph MF. Axisymmetric time-domain transmitting boundaries. J Eng Mech 1994;120(1):25–42.
[46] Liu J-B, Wang Z-Y, Du X-L, Du Y. Three dimensional viscous-spring artificial boundaries in time domain for wave motion problems(in Chinese). Eng Mech 2005;22(6):46–51.
[47] Huang J, Zhao M, Du X. Non-linear seismic responses of tunnels within normal fault ground under obliquely incident p waves. Tunn Undergr Space Technol 2017;61:26–39.
[48] Kuhlemeyer RL, Lysmer J. Finite element method accuracy for wave propagation problems. J Soil Mech Found Div 1973;99(5):421–7.
[49] Liu H, Fan Z, Wei H. Gpu rasterization based octree fast generation algorithm for terrain modeling. In: 2013 IEEE international geoscience and remote sensing symposium - iGARSS.. 2023, p. 282–5, IGARSS 2013 - 2013 IEEE International Geoscience and Remote Sensing Symposium.
[50] Assimaki D. Effects of local soil conditions on the topographic aggravation of seismic motion: Parametric investigation and recorded field evidence from the 1999 athens earthquake. Bull Seismol Soc Am 2005;95(3):1059–89.
[51] Gao Y-F, Zhang N, Li D-Y, Liu H-L, Cai Y-Q, Wu Y-X. Effects of topographic amplification induced by a U-shaped canyon on seismic waves. Bull Seismol Soc Am 2012;102(4):1748–63.
[52] Brussels. Eurocode 8: Design of structures for earthquake resistance - Part 5: Foundations, retaining structures and geotechnical aspects. CEN European Committee for Standardisation; 2003.
[53] Geli L, Bard P-Y, Jullien B. The effect of topography on earthquake ground motion: A review and new results. Bull Seismol Soc Am 1988;78(1):42–63.